TOPEX/Poseidon Microwave Radiometer (TMR): I. Instrument Description and Antenna Temperature Calibration

Christopher S. Ruf, *Senior Member, IEEE,* Stephen J. Keihm, and Michael A. Janssen

***Abstract*—The TOPEX/Poseidon Microwave Radiometer (TMR) is a three-frequency radiometer flown on the TOPEX/Poseidon (T/P) satellite in low Earth orbit. It operates at 18, 21, and 37 GHz in a nadir-only viewing direction which is co-aligned with the T/P radar altimeters. TMR monitors and corrects for the propagation path delay of the altimeter radar signal due to water vapor and nonprecipitating liquid water in the atmosphere. This paper describes the TMR instrument and the radiometric instrument calibration required to derive antenna temperature (T_A) from the raw digital data. T_A precision of 0.4°K is predicted on orbit in all expected thermal environments. T_A accuracy of 0.5–0.6°K is expected following a post-launch field calibration campaign. These performance figures represent a significant improvement over those of the Seasat and Nimbus-G Scanning Multichannel Microwave Radiometer on which TMR is based. The improvements are the result of specific hardware design and calibration changes. Hardware changes include a redesigned feed horn, to reduce impedance mismatches, and the addition of radomes over the feed and sky horns, to reduce thermal variations. Calibration changes involve more extensive temperature cycling and data analysis during thermal/vacuum testing.**

I. Introduction

THE primary instruments on the TOPEX/Poseidon (T/P) satellite are two radar altimeters, designed to determine the radial distance between the satellite and the ocean surface by a precise measurement of the round trip time of flight of the radar signal. This distance can be translated into a measurement of the sea level along the T/P ground track given accurate knowledge of the location of the satellite in earth orbit. The nominal satellite altitude of 1375 km and orbit repeat time of 9.9 d result in a global map of the sea level on a grid spaced 316 km apart at the equator and updated every 9.9 d [1].

A. Radar Altimeter Errors

There are three general categories of uncertainties associated with the T/P maps of sea level. The first involves the Precision Orbit Determination (POD) algorithm, which locates the spacecraft center of mass relative to a reference Earth geoid. Errors with the POD include inaccuracies in the orbital gravity field, along with a number of other smaller unknowns. Another category of errors involves the inaccuracies of the radar measurements themselves. Radar errors include electronic noise from sources such as time sampling, digitization, and the noise figure of the radar receiver and drifts in instrumental bias. The third category of errors involves inaccuracies in the correction of the time of flight of the radar signal due to propagation effects. The ionosphere, dry air in the atmosphere, and water vapor, primarily in the troposphere, will all delay the radar signal, relative to its time of flight in a vacuum.

A correction is made for the ionospheric delay by using two radar frequencies, at 5.3 and 13.6 GHz, which are affected differently. The integrated free electron content beneath the satellite can be estimated from the difference in time of flight at the two frequencies [2]. The dry atmosphere delay can be estimated from interpolated grids of global surface barometric pressure which are available, e.g., from the Fleet Numerical Oceanography Center (FNOC) [3]. The delay introduced by water vapor is determined from direct TOPEX/Poseidon Microwave Radiometer (TMR) measurements of the integrated water vapor content lying between the spacecraft and the Earth surface [4]. The apparent increase in path length due to the water vapor, relative to propagation in dry air, typically ranges from 5–10 cm in cold, dry climates to 30–50 cm under warm, humid conditions. This effect will henceforth be referred to as the wet tropospheric *path delay*. After correction, the residual uncertainty in sea level due to atmospheric water vapor should be less than 1.2 cm.

B. Previous Wet Tropospheric Path Delay Corrections

Other satellite altimeters have all attempted to correct for the path delay due to water vapor. The Seasat radar altimeter operated in conjunction with the Scanning Multichannel Microwave Radiometer (SMMR) [5]. In this case, the altimeter's radar signal propagated in the nadir direction, whereas the SMMR antenna was directed 42° away from nadir [6]. Thus, while SMMR was estimated to retrieve nadir normalized path delay with a precision of 1.5 cm along its line of propagation [7], the error in its path delay retrieval relative to the actual line of propagation of the radar signal

Manuscript received September 7, 1993; revised February 17, 1994. This work was supported in part by the National Aeronautics and Space Administration.

C. S. Ruf is with the Department of Electrical Engineering, Pennsylvania State University, University Park, PA 16802 USA.

S. J. Kiehm is with Ball Corporation under contract to the Jet Propulsion Laboratory, California Institute of Technology, Pasadena, CA 91109 USA.

M. A. Janssen is with the Jet Propulsion Laboratory, California Institute of Technology, Pasadena, CA 91109 USA.

IEEE Log Number 9407084.

is estimated at 2.5 cm [8]. The GEOSAT altimeter has no companion microwave radiometer and must rely on other estimates of the wet tropospheric path delay. For example, tropical climatology records compiled from SMMR data show typical monthly standard deviations in the path delay of 1.5–2.5 cm about monthly averages made over several years [9]. However, monthly standard deviations during the El Nino-Southern Oscillation event in 1982–1983 exceeded 12 cm [9] and typical variations on time scales of shorter than one month should exceed the 1.5–2.5 cm. Another option for correction of GEOSAT data makes use of the climatological model developed by the European Centre for Medium Range Weather Forecasting. This model combines observations with numerical weather predictions to estimate temperature and humidity fields on a 40 km grid with 15 vertical cells across the Northeast Atlantic and European coast. The accuracy of wet tropospheric path delay estimates derived from these fields is estimated at 10% of the path delay [10]. This corresponds to 1–2 cm under typical conditions, but would degrade significantly in high humidity or anomalous weather. The ERS-1 satellite is instrumented with both a radar altimeter and a nadir viewing microwave radiometer. The radiometer operates at 23.8 and 36.5 GHz and the accuracy of its wet tropospheric path delay retrieval is estimated to be 2 cm [11].

The above examples illustrate the difficulty of achieving a 1.2 cm accuracy in the wet tropospheric path delay correction. A dedicated microwave radiometer is needed, co-aligned with the radar altimeter antenna and operating at frequencies which optimize the retrieval of atmospheric water vapor. For this reason, the T/P project incorporated TMR into its mission design.

C. Outline of Paper

TMR is a modified version of the SMMR instrument. A full description of SMMR is available in [6], [12], [13]. The hardware modifications for TMR were motivated in part by the change in mission objectives of T/P and in part by calibration problems that SMMR experienced on orbit [14], [15]. Section II of this paper begins with a brief review of these calibration problems. This is followed by a detailed description of the modifications made to TMR which were intended to address the problems. Section II concludes with a summary of the overall calibration approach used by TMR.

Section III describes the radiometric instrument calibration required to derive antenna temperature (T_A) from the raw digital data. This procedure is referred to as T_A calibration. The section begins with a description of the T_A calibration approach used by TMR. This approach is a modification to the similar approach which was used with SMMR and which is described in detail in [13]. Next, results of the pre-launch calibration and validation of the T_A algorithm are presented which were performed during thermal/vacuum (T/V) testing. The final step in the T_A calibration involves a post-launch calibration and validation program which uses underflight measurements of downwelling brightness temperature and surface meteorology at selected island sites to verify the T_A calibration and "fine tune" the overall TMR wet tropospheric path delay retrieval algorithm. This program is briefly reviewed here in the context of the T_A calibration algorithm. It is described in much greater detail in [16].

II. Instrument Description

A. Review of SMMR Calibration

T_A calibration for SMMR was performed by measuring the radiometer response to hot and cold reference T_As at regular intervals during operation. A number of problems arose during SMMR operation which made absolute calibration of the brightness temperature images difficult. An excellent review of these problems is given by [15]. Some of the problems involved the coupling between horizontal and vertical polarization due to the antenna scan geometry—these will not affect TMR and will not be discussed here. Problems with SMMR which may also affect TMR involve the MFFH design and the hardware implementation of the hot/cold antenna calibration. The very wide bandwidth of the MFFH (6.6–37.0 GHz) necessitated compromises in its operation at individual SMMR frequencies. For example, the flare angle of the feed horn was larger than optimal at the higher frequencies in order to accommodate the lower frequencies in a reasonable size. At the higher frequencies, this produced additional phase errors in the aperture plane of the feed, a poorer impedance match at the output ports of the feed, and a ripple in the center of the main reflector illumination pattern [21]. The edge taper used to illuminate the main reflector was also a compromise, between the desire for high spatial resolution and for high beam efficiency. The taper used resulted in a significant amount of spillover past the main reflector and scattering from the six rods supporting the main reflector. This degraded the beam efficiency of the antenna.

The use of microwave ferrite switches, extended runs of waveguide, and separate sky horn antennas to provide hot and cold points for the T_A calibration introduced a number of problems [14]. The cold point measured by the radiometer had to be estimated from a radiative transfer model for propagation of the incoming cold space brightness temperature ($\approx$2.7°K) through the subsequent hardware. Similarly, the radiometer measurements made with the ferrite switch matrix in the MFFH viewing mode included radiative transfer effects through the MFFH, the waveguide run between the MFFH and the switch, and the switch itself. The hot point measurement made while viewing a blackbody waveguide termination also included propagation through the ferrite switch. Errors in the radiative transfer model used for these effects produced errors in the T_A calibration which were sensitive to variations in the physical temperature of the microwave hardware. The model errors resulted from an incomplete cycling of the instrument physical temperatures during the pre-flight T/V calibration procedure. The SMMR calibration hardware encountered significant variations in its physical temperature on orbit over periods of minutes due to solar heating and the

Fig. 1. The TMR instrument.

TABLE I
TMR ENGINEERING SPECIFICATIONS

FREQUENCY (GHz)	18	21H	21V	37
HPBW (deg)	1.86	1.56	1.59	0.98
Beam Efficiency (%)	91.1	89.3	87.4	90.5
Predetection Bandwidth (MHz)	100	100	100	100
Integration Time (s)	1.0	1.0	1.0	1.0
Radiometer Noise, ΔT (K)	0.26	0.27	0.27	0.27
Calibrated T_B Accuracy (K)	0.77	0.74	0.79	0.71

calibration was degraded as a result [15]. One other problem with the cold point calibration measurements for SMMR was caused by the sun entering the main beam of the sky horn [6].

B. TMR Instrument Modifications

TMR is a modified version of a backup SMMR flight instrument which was not used during the Seasat or Nimbus programs. A picture of the instrument is shown in Fig. 1 and a block diagram in Fig. 2. A summary of the instrument engineering specifications for TMR is given in Table I. Several of the changes made to SMMR followed naturally from the specific requirements of the T/P mission. The antenna scanning mechanism was removed since TMR is strictly a nadir-viewing instrument. The lower frequency channels (6.6 and 10.7 GHz) were removed since they are not needed to estimate wet tropospheric path delay over the ocean [17]. The polarization select switch for the 18.0 GHz channel is set permanently in the horizontal polarization position and the vertical polarization output port of the MFFH at this frequency is terminated with a matched load. Similarly, the vertical polarization radiometer channel at 37.0 GHz was removed and this MFFH port was also terminated with a matched load, leaving a single 37.0-GHz radiometer connected to the horizontal port of the MFFH. These modifications were possible because the nadir viewing geometry eliminates any significant polarization sense. (The effects of a small anisotropy which is present in the cross-wind/along-wind surface emissivity [18] is negligible, provided all three TMR channels are polarized in the same direction.) Whereas SMMR used one radiometer at 21.0 GHz to monitor both polarizations, TMR has two identical, independent radiometers at 21.0 GHz, one connected to each of the two polarization output ports from the MFFH. Each of these radiometers has a ferrite switch matrix assembly with the polarization select switch set permanently in the position which is connected to the MFFH. Only one of the 21.0 GHz channels will be turned on initially. The other will serve as a back up in case of failure. Only the 21.0 GHz channel is redundant because it is critical to the T/P mission. TMR path delay retrieval performance would degrade but still be useful if either of the other two, but not the 21.0 GHz, channels fails [17]. Another straightforward modification to the SMMR design involved the positioning and pointing geometry of the sky horns. A sky horn location and pointing geometry was selected which should prevent the sun from entering a cone centered on its boresight and with a half angle of 60°. This lies well outside of the nominal sky horn HPBW of 24°.

The MFFH used for SMMR is built in three sections. The top section starts at the 5.25-in diameter circular aperture of the feed horn and tapers in with a ring-loaded corrugated conical horn to a circular waveguide with coaxial output ports for the 6.6 GHz channels. The next section is a circular waveguide with output ports for the 10.7 GHz channels, followed by a tapered circular-to-rectangular waveguide transition. The last section begins with output ports at 18.0 and 21.0 GHz, then tapers and transitions to a rectangular waveguide with output ports at 37.0 GHz. For TMR, the top section has been replaced by a similar ring-loaded corrugated horn with a narrower flare angle which only opens out to a circular aperture diameter of 4.0 in. The middle section has been replaced by a tapered circular-to-rectangular waveguide transition with no output ports. The final section has been left unchanged. A cross sectional drawing of the TMR MFFH is shown in Fig. 3.

The reduced flare angle of the TMR MFFH provides a more gradual transition at the higher frequencies from waveguide

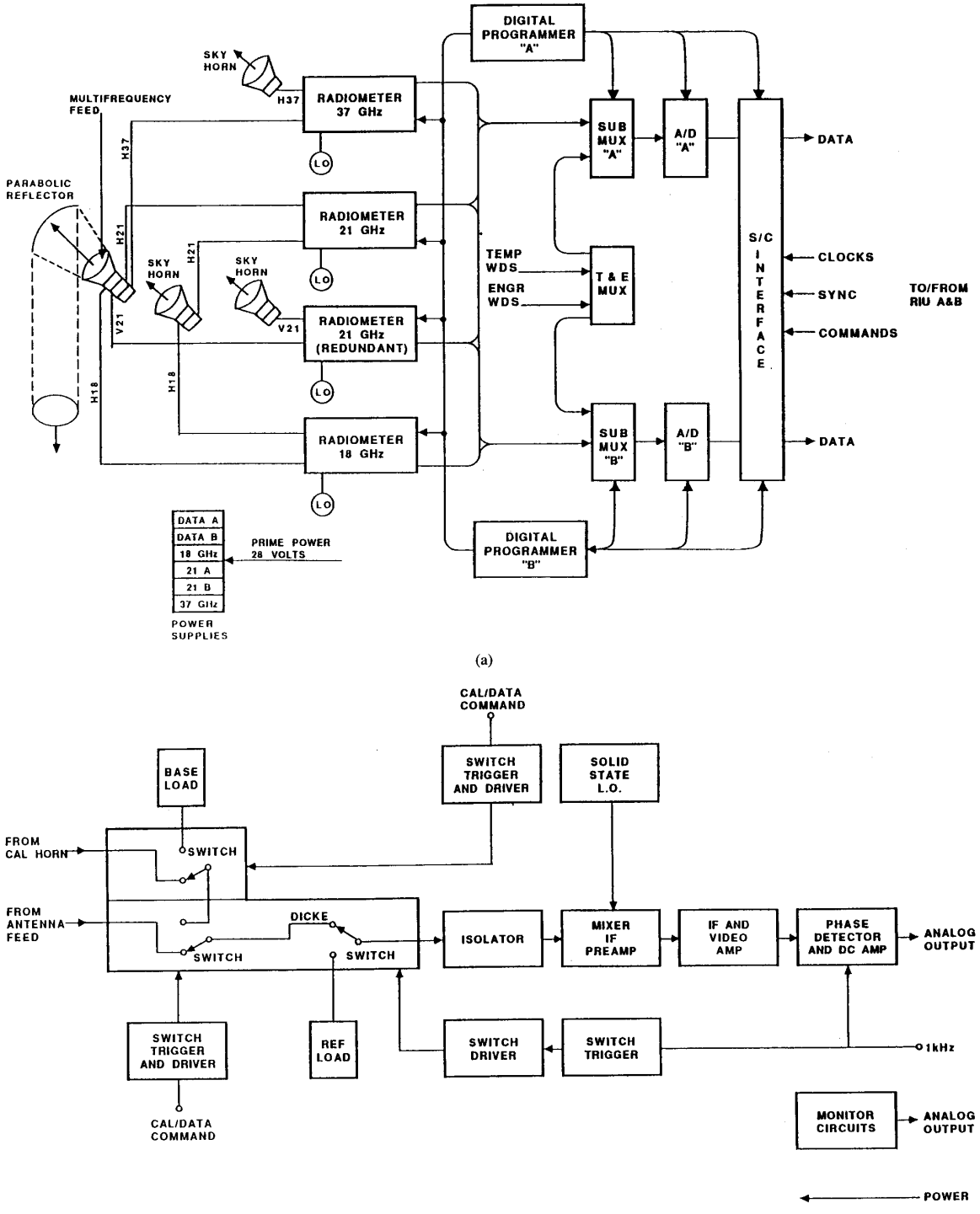

Fig. 2. TMR functional block diagrams. (a) System design and (b) typical radiometer channel.

to free space propagation. This reduces the phase error at the aperture plane, which in turn improves the feed radiation pattern and the impedance match at the MFFH output ports. A sample of the MFFH radiation pattern at 21.0 GHz before and after the modification to the flare angle is shown in Fig. 4. The SMMR feed pattern has a ripple across the center which has

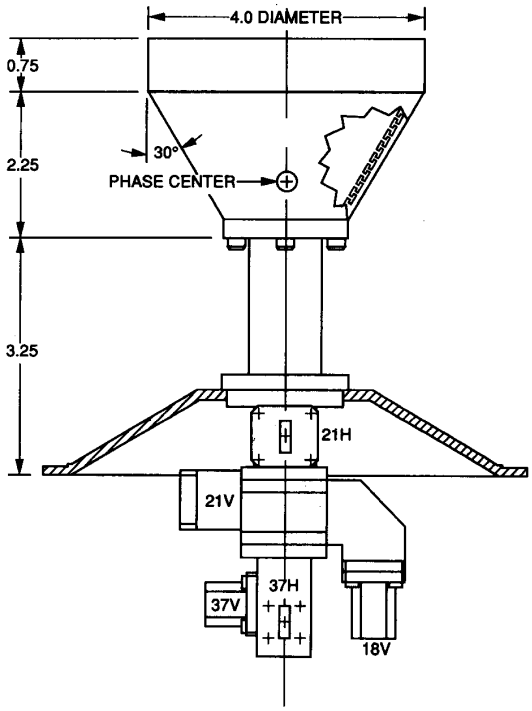

Fig. 3. TMR multi-frequency feed horn (MFFH) (note: dimensions shown are in in).

been eliminated. The power level of the feed pattern at ±41° corresponds to the edge illumination of the main reflector. This level has also been reduced with the TMR MFFH. The under-illumination of the main reflector will tend to increase the HPBW of the complete TMR antenna pattern and decrease its overall far sidelobe level by reducing the spillover past the reflector and the scattering off of the six reflector support rods. The main reflector used for TMR is identical to those used for SMMR. A summary of the TMR antenna performance is given in Table II, along with a comparison to earlier SMMR performance specifications. A number of the TMR specifications are described in greater detail in [4]. The HPBW and resulting Earth footprint have increased with TMR by approximately 5%. The beam efficiency has increased on average by 2.4%. Most significantly, the percentage of power received from the far sidelobes of the antenna which will lie off the earth during the mission has been reduced from 5.7–10.1% to 0.4–0.7%. This will greatly improve the accuracy of the sidelobe corrections in the brightness temperature calibration algorithm [4].

Radomes were added to the TMR MFFH and sky horns to reduce short term fluctuations in the physical temperatures of these antennas caused by solar heating. These radomes are flat 3/8-in thick pieces of polystyrene (Styrofoam) with a mass density of 2 lbs/ft^3. They are positioned in front of the horns, perpendicular to their central axis and wide enough to block all incident sun light. Pre-flight thermal analysis indicates that the radomes will significantly reduce the expected on orbit variations in the MFFH and sky horn temperatures. A number of tests were conducted to estimate the effects of these radomes on TMR performance.

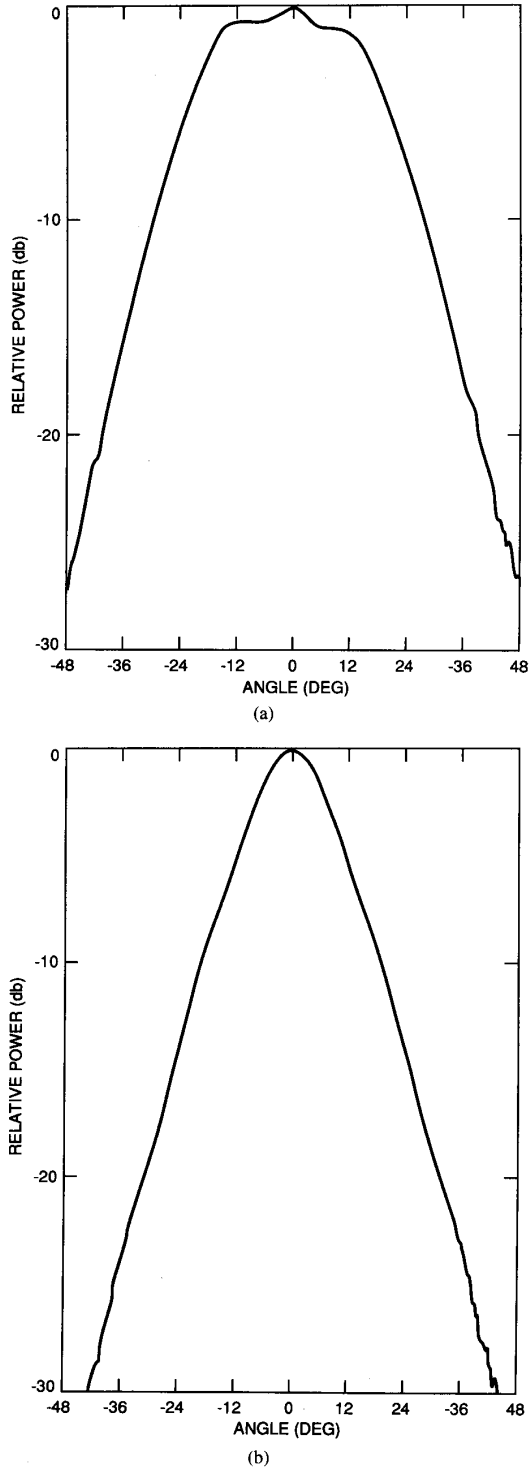

Fig. 4. MFFH radiation patterns at 21.0 GHz, vertical polarization, H-plane cut. (a) with original SMMR flare angle and (b) with narrower TMR flare angle. Reduced phase error at the higher frequencies lowers the ripple in the pattern and improves the impedance match.

TABLE II
TMR ANTENNA PERFORMANCE (AND COMPARISON WITH SMMR)

	TMR	SMMR
MFFH Performance		
Return Loss at output ports (dB)		
18.0 GHz	28	21
21.0 GHz, H-pol	>40	16
21.0 GHz, V-pol	23	17
37.0 GHz	32	23
Reflector edge illumination (dB)		
18.0 GHz	-24	-23
21.0 GHz, H-pol	-23	-21
21.0 GHz, V-pol	-23	-21
37.0 GHz	-29	-26
Reflector Performance		
Half Power Beam Width (deg)		
18.0 GHz	1.86	1.81
21.0 GHz, H-pol	1.56	1.49
21.0 GHz, V-pol	1.59	1.50
37.0 GHz	0.98	0.93
Beam efficiency[1] (%)		
18.0 GHz	91.1	88.7
21.0 GHz, H-pol	89.3	85.8
21.0 GHz, V-pol	87.4	84.2
37.0 GHz	90.5	90.0
Integrated on-earth far sidelobe level[2] (%)		
18.0 GHz	2.78	≈1.8[3]
21.0 GHz, H-pol	2.47	≈2.4[3]
21.0 GHz, V-pol	3.16	≈2.7[3]
37.0 GHz	2.15	≈1.5[3]
Integrated off-earth sidelobe level[4] (%)		
18.0 GHz	0.49	≈6.8[3]
21.0 GHz, H-pol	0.29	≈9.0[3]
21.0 GHz, V-pol	0.30	≈10.1[3]
37.0 GHz	0.37	≈5.7[3]

Notes: 1. Percentage of power received inside 2.5 × HPBW.
2. Percentage of power received between 10° and 55° off boresight.
3. Estimated from measured SMMR beam efficiencies and model fit to SMMR antenna patterns.
4. Percentage of power received outside 55° off boresight.

Electrical radome performance was estimated using an available ground based water vapor radiometer (WVR) operating at 20.7 and 31.4 GHz. T_A was measured while viewing the zenith sky both with and without the radome. For the determination of insertion loss, the radome was set against a flat metal reflecting plate angled at 45° relative to both the WVR antenna boresight and zenith. This reduced the effects of reflections from the radome. For the characterization of reflections, the radome was positioned directly in front of the WVR antenna and perpendicular to its boresight. The distance between the radome and the WVR antenna was then varied to measure standing waves in T_A due to reflections from the radome. The insertion loss of the polystyrene was determined to be 0.2% ± 0.1%/in of radome thickness at both 20.7 and 31.4 GHz. The standing wave characterization consisted of a Fourier analysis of the variation in T_A with radome position, to extract that harmonic which was due to reflections from the radome. The results of the standing wave test are summarized in Table III. The effects of reflections are substantially less than that of general purpose polystyrene, which has a density of 15–20 lbs/ft^3 and a dielectric constant of approximately 2.6 [19]. Low density polystyrenes such as are used here have dielectric constants in the range 1.03–1.16 [20].

The effects of ultraviolet (UV) radiation on the radome material were also tested. A sample of the radome was exposed to a 75 watt Xenon lamp producing ≈1400 W/m^2 of UV radiation at the center and ≈300 W/m^2 at the edge of a 1 inch spot. The expected incident UV radiation on orbit is 118 W/m^2 with intermittent exposure by the sky horn radome during approximately 12% of the mission and at grazing angles of 60° or greater. The MFFH radome will be exposed during approximately 4% of the mission and at grazing angles of 42° or greater. The polystyrene sample was exposed for a total of 2.7 times the mission exposure level for the sky horn radome (7.8 times the MFFH radome exposure). The 1-in spot discolored almost immediately, from an initial white to a yellowish-brown color. No further changes were observed. Subsequent to the exposure, a microscopic examination found that the discoloration extended approximately 0.0015 in into the material, uniformly across the 1-in spot. This indicates that the discoloration is a self-limiting process. Additionally, an RF transmission test after exposure found no significant change and a study of the impact of discoloration on the radome thermal balance was satisfactory.

C. TMR Calibration Procedures

TMR calibration can be divided into three stages. The first stage is T_A calibration. Raw digital counts are recorded by TMR with the ferrite switch matrix at the input to the radiometer electronics directed to each of the matched load termination (hot point), sky horn (cold point), and MFFH (intermediate earth viewing data point) source positions. The operational sequence of data taking is 14 1-s earth observations, followed by a single 1-s hot point measurement, then another fourteen 1ts earth observations, then a single 1–s cold point measurement. This T_A calibration algorithm is described in detail in the following section.

The second stage of TMR calibration deconvolves the effects of the antenna pattern to estimate the brightness temperature of the earth in the direction of the TMR antenna main beam. This brightness temperature calibration algorithm is discussed in [4]. The final stage of calibration involves the wet tropospheric path delay retrieval algorithm which estimates vertical path delay from the nadir brightness temperatures. The retrieval algorithm is described in [17].

III. ANTENNA TEMPERATURE CALIBRATION

A. Hardware Radiative Transfer Model

The TMR front-end ferrite switch assemblies allow for three different input sources: the Earth viewing antenna, the cold sky viewing calibration horn, and the hot load at instrument ambient temperature. The system temperature detected by the TMR back-end in each of these cases is determined by the radiative transfer of the signal from its input source to the output of the ferrite switch assembly.

The model used for the signal flow from the Earth viewing antenna input source is shown in Fig. 5. In the figure, α_f, α_w, and α_s are the numeric power transmission coefficients

TABLE III
TMR RADOME STANDING WAVE TEST RESULTS

Thickness (in)	freq (GHz)	T-a pk-to-pk (K)[1]	T-sky (K) w/o RADOME[2]	T-sky (K) w/ RADOME[3]
1/4	20.7	0.07	19.6	19.7
	31.4	0.15	14.7	15.2
3/8	20.7	0.09	19.9	20.1
	31.4	0.07	15.2	15.9
1/2	20.7	0.11	19.9	20.4
	31.4	0.20	15.4	16.1
5/8	20.7	0.25	20.0	20.3
	31.4	0.35	15.6	16.1

(All results are for a flat sheet of polystyrene, 2 lbs/ft^3 density.)

Notes: 1. Fourier component of antenna temperature corresponding to half wavelength standing waves due to radome reflection.
2. Zenith viewing antenna temperature without radome
3. The mean antenna temperature viewing the zenith sky through the radome averaged over the standing waves

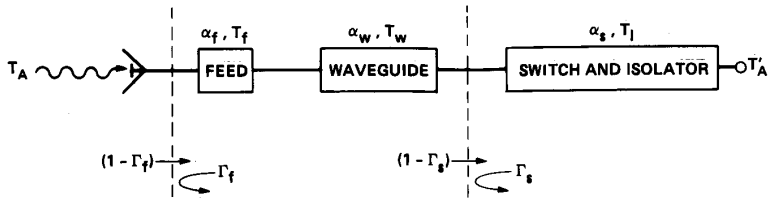

Fig. 5. Model used for the radiative transfer of thermal emission through the TMR front end hardware.

through the antenna feed, the waveguide from the feed to the ferrite switch, and the ferrite switch assembly, respectively. T_f, T_w, and T_I are the physical temperatures of these same components (in units of degrees K), and Γ_f and Γ_s are the numeric power reflection coefficients at the feed and ferrite switch, respectively. Let T'_A denote the effective antenna temperature leaving the output port of the front end. It is given by

$$\begin{aligned} T'_A = {} & T_A(1-\Gamma_f)(1-\Gamma_s)\alpha_f\alpha_w\alpha_s \\ & + T_f(1-\alpha_f)(1-\Gamma_s)\alpha_w\alpha_s(1+\Gamma_f\alpha_f) \\ & + T_w(1-\alpha_w)(1-\Gamma_s)\alpha_s(1+\Gamma_f\alpha_f^2\alpha_w) \\ & + T_I[(1-\alpha_s)+\alpha_s|\Gamma_s^{1/2} \\ & + (1-\Gamma_s)\Gamma_f^{1/2}\alpha_f\alpha_w e^{j\phi}|^2] \end{aligned} \tag{1}$$

where T_A is the true antenna temperature referenced to the input of the feed horn and ϕ is twice the electrical phase separation between the feed horn and the antenna input to the ferrite switch assembly.

The model used for the signal flow from the calibration horn is the same and the resulting equation of radiative transfer is similar to that derived above, except that α_h, α_{h-w}, and α_{h-s} are the corresponding transmission coefficients along the calibration path, T_h and T_{h-w} are the temperatures of the calibration horn and connecting waveguide, respectively, and Γ_h are Γ_{h-s} are the reflection coefficients at the horn and ferrite switch. If T'_c is the total thermal emission leaving the output port of the ferrite switch assembly and $T_c \approx 2.7°$K is the input source to the calibration horn, then

$$\begin{aligned} T'_c = {} & T_c(1-\Gamma_h)(1-\Gamma_{h-s})\alpha_h\alpha_{h-w}\alpha_{h-s} \\ & + T_h(1-\alpha_h)(1-\Gamma_{h-s})\alpha_{h-w}\alpha_{h-s} \\ & \cdot(1+\Gamma_h\alpha_h) \\ & + T_{h-w}(1-\alpha_{h-w})(1-\Gamma_{h-s})\alpha_{h-s} \\ & \cdot(1+\Gamma_h\alpha_h^2\alpha_{h-w}) \\ & + T_I[(1-\alpha_{h-s})+\alpha_{h-s}|\Gamma_{h-s}^{1/2} \\ & + (1-\Gamma_{h-s})\Gamma_h^{1/2}\alpha_h\alpha_{h-s}e^{j\phi_h}|^2] \end{aligned} \tag{2}$$

where ϕ_h is twice the electrical phase separation between the calibration horn and the ferrite switch input port. The exact value used for the cosmic background brightness temperature, T_C, varies with frequency due to the strict proportionality assumed between brightness temperature and radiated power. While the equivalent physical temperature of the cosmic background radiation is 2.735°K in the microwave regime, independent of frequency, the brightness temperature varies due to a frequency dependent departure of the full Planck blackbody radiation expression from the Rayleigh-Jeans approximation. This departure is approximately constant over the range of expected brightness temperatures viewed by the TMR main reflector. However, the full Planck correction is different near the 2.7°K scene viewed by the cold sky horn. This difference in the correction is accounted for by adjusting T_C. This forces a constant Planck correction at all scene brightness temperatures and allows the TMR gain to be computed correctly from the hot and cold digital counts.

The signal flow from the hot load is given by

$$T_H' = T_I \tag{3}$$

where T_H' is the output of the ferrite switch. This follows since the hot load is connected directly to the switch and both are at physical temperature T_I.

The TMR is a Dicke Radiometer which is sensitive to the difference between the thermal emission from an input source and from an ambient load. Digital measurements C_N ($N = A$, C, or H) are made for the three input sources (Antenna, Cold sky, or Hot load). These measurements are related to the output thermal emission derived above by

$$C_N = G(T_N' - T_I) + C_0 \tag{4}$$

where $N = A$, C, or H, G is the gain of the radiometer in units of digital counts/degree, and C_0 is a possible offset.

The measured thermal emission, T_A', is found by combining (3) with (4) for the cases $N = A$ and $N = C$, giving

$$T_A' = \frac{(C_A - C_H)(T_I - T_c')}{(C_H - C_C)} + T_I. \tag{5}$$

The antenna temperature, T_{A0}, is found by inverting (1) with respect to the measurement of T_A' given by (5). This results in an estimate of the antenna temperature described by

$$\begin{aligned} T_{A0} = {} & \frac{C_A - C_H}{C_H - C_C}(a_1 T_c + a_2 T_h + a_3 T_{h-w} + a_4 T_I) \\ & + a_5 T_f + a_w T_w + a_6 T_I \end{aligned} \tag{6}$$

where

$$\begin{aligned} a_1 &= -[(1-\Gamma_h)(1-\Gamma_{h-s})\alpha_h \alpha_{h-w}\alpha_{h-s}]/D \\ a_2 &= -[(1-\alpha_h)(1-\Gamma_{h-s})\alpha_{h-w}\alpha_{h-s} \\ &\quad \cdot (1+\Gamma_h\alpha_h)]/D \\ a_3 &= -[(1-\alpha_{h-w})(1-\Gamma_{h-s})\alpha_{h-s} \\ &\quad \cdot (1+\Gamma_h\alpha_h^2\alpha_{h-w})]/D \\ a_4 &= \{1-[(1-\alpha_{h-s})+\alpha_{h-s}|\Gamma_{h-s}^{1/2} \\ &\quad + (1-\Gamma_{h-s})\Gamma_h^{1/2}\alpha_h\alpha_{h-w}e^{j\phi_h}|^2]\}/D \\ a_5 &= -[(1-\alpha_f)(1-\Gamma_s)\alpha_w\alpha_s(1+\Gamma_f\alpha_f)]/D \\ a_w &= -[(1-\alpha_w)(1-\Gamma_s)\alpha_s(1+\Gamma_f\alpha_f^2\alpha_w)]/D \\ a_6 &= \{1-[(1-\alpha_s)+\alpha_s|\Gamma_s^{1/2}+(1-\Gamma_s) \\ &\quad \cdot \Gamma_f^{1/2}\alpha_f\alpha_w e^{j\phi}|^2]\}/D \end{aligned}$$

and

$$D = (1-\Gamma_f)(1-\Gamma_s)\alpha_f\alpha_w\alpha_s.$$

In practice, the thermal emission from the waveguide between the MFFH and the ferrite switch assembly is negligible, and a_w is taken to be zero. The remaining calibration coefficients, $a_1 - a_6$, have been estimated from data measured during T/V testing of TMR.

Equation (4) assumes a purely linear relationship between the digital outputs (voltages) and temperature inputs (powers). Actual microwave radiometers exhibit a small nonlinearity, typically due to amplifier compression and/or non-"square-law" detector behavior. Analysis of the measurements made during T/V testing is discussed below. The analysis suggests the form of the nonlinearity correction which should be used. This second order effect is well modeled by a quadratic term which is centered about a nonzero T_A. In addition, the degree of nonlinearity is strongly correlated with the instrument temperature. Since the nonlinearity at all temperatures is small, a linear dependence on instrument temperature is sufficient to model this correlation. The quadratic correction to T_A is given by

$$T_A = T_{A0} + a_7(T_{A0} - a_8)^2 + a_9 \tag{7}$$

where

T_A is the final, fully calibrated antenna temperature
T_{A0} is given by (6)

and where

$$a_i = b_{i1}T_I + b_{i2} \text{ for } i = 7, 8, \text{ and } 9 \tag{8}$$

where

b_{ij} are constants derived from the T/V test data
T_I is the TMR instrument temperature

B. Thermal/Vacuum Antenna Temperature Calibration/Validation

1. Overview of Thermal/Vacuum Test: The T/V test consists of a series of calibration runs with the TMR operating at different physical temperatures. Temperature controlled black body targets are positioned in front of both the MFFH and the sky horns. These targets are also run at different temperatures. A calibration run consists of a set of digital counts recorded while the radiometer is switched to look at each of the MFFH target, the sky horn target, and an internal ambient matched load.

Physical temperature variations are controlled differently for different parts of the hardware. The targets are controlled by LN_2 and gaseous N_2 manifolds soldered to the back sides of the heatsinks surrounding the absorbing material. The overall instrument temperature is controlled by similarly heated and cooled jackets attached to the sides of the instrument, where the passive radiant coolers are normally attached in flight. The temperatures of individual parts of the microwave front-end electronics are independently controlled by small electric heater strips. There are 14 of these heaters, located as follows: 1) and 2) around the outside of the upper MFFH; 3) around the throat of the MFFH; 4) midway along the 18 GHz waveguide run between the MFFH and the instrument ferrite switch assembly; 5)–7) same as 4) for the 21H, 21V, and 37 GHz channels, respectively; 8) around the outside of the single cal horn shared by the 18 and 21H GHz channels; 9) and 10) same as 8) for the 21V and 37 GHz channels, respectively; 11) midway along the waveguide run between the cal horn for the 18 GHz channel and the instrument ferrite switch assembly; and 12)–14) same as 11) for the 21H, 21V, and 37 GHz channels, respectively.

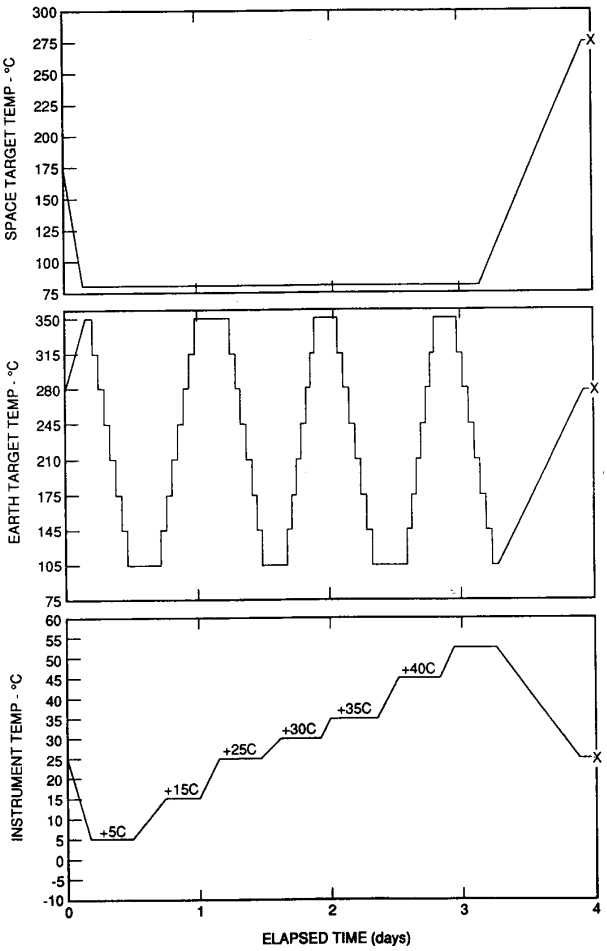

Fig. 6. T/V test temperature time lines for overall instrument and antenna temperature variations.

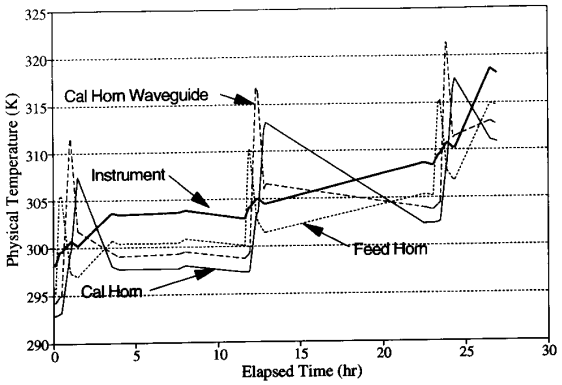

Fig. 7. T/V test measured temperature variations of individual microwave components.

Temperature variations can be divided into three parts. In the first part, the instrument temperature, T_I, is varied from 5° to 50°C, in steps of 5° or 10°C, by controlling the large temperature jackets attached to the sides of the instrument. At each plateau, the MFFH target temperature is varied from 100° to 350°K in 35°-K steps and the sky horn target temperature is maintained at ≈80°K. This sequence is illustrated in Fig. 6. No independent control is maintained of the individual heater strips; they are always off and the assemblies they are attached to typically had monotonic gradients running from the instrument temperature to the target temperature. At each instrument and target temperature, a calibration run was made after the temperature had stabilized.

The second part of the temperature variation procedure occurred at each instrument plateau and at a fixed MFFH target temperature of either 100K or 240 K. The individual heater strips were turned on in the following sequence: 1) MFFH and MFFH waveguide heaters (#1–7) turned on with temperature set point 10°K higher than the overall instrument temperature; 2) Heaters #1–7 turned off and heaters #11–14 (waveguides between sky horn and instrument) turned on with a temperature set point also 10°K above the instrument; and (3) Heaters #11–14 turned off and heaters #8–10 (sky horn) turned on with a set point 10°K above the instrument. The effect which these heater adjustments had on the physical temperatures of the microwave components is shown in Fig. 7, which plots actual temperatures recorded during the test. A calibration run was performed before step 1 and after each of steps 1–3. These independent variations in component temperatures allowed the effects of thermal emission from the components to be isolated and quantified.

The third part of the test consisted of a set of calibration measurements made while the cold sky horn target temperature was maintained at 296°K. Instrument and MFFH target temperatures were also at ambient temperature during this time.

2. T/V Data Reduction and Analysis: T/V data reduction can be divided into three segments: (1) the calibration coefficients related to thermal emission from and attenuation by the MFFH, cold sky horn, waveguide to the cold sky horn, and Dicke and calibration ferrite switch assemblies $(a_2 - a_6)$ are estimated by multi-linear regression of data taken when their temperatures were varied in a linearly independent manner; (2) the calibration coefficient relating to the dependence of T_A on the cold sky horn target temperature (a_1) is estimated by linear regression of data taken when the cold sky horn target was at ambient, combined with an equal quantity of data selected from the large database with the target at 80°K; and (3) the calibration coefficients relating quadratic correction terms to the instrument temperature $(b_{71} - b_{92})$ are estimated by linear regression of the best fit quadratic corrections at each instrument temperature. Step 1 requires an estimate of the result of step 2. Likewise, step 2 requires that the coefficients from step 1 are known. In practice, these steps are iterated until the coefficient estimates converge. Step 3 is then evaluated using these coefficients.

a. Multilinear estimate of hardware emission: Equation (6) can be rewritten for the case of N different configurations of the instrument and MFFH target physical temperatures in the

TABLE IV
TMR ANTENNA TEMPERATURE LOSS COEFFICIENTS

	TMR Frequency (GHz)			
	18	21H	21V	37
		Sky horn target coefficients		
a_1	-1.06502	-1.051537	-1.166330	-0.967654
		Component losses and reflections (t/- covariance errors)		
a_2	-0.111 ± 5%	-0.037 ± 20%	-0.038 ± 11%	-0.051 ± 10%
a_3	-0.111 ± 5%	-0.037 ± 20%	-0.038 ± 11%	-0.051 ± 10%
a_4	1.290 ± 2%	1.121 ± 3%	1.251 ± 3%	1.065 ± 2%
a_5	-0.280 ± 7%	-0.176 ± 13%	-0.101 ± 24%	-0.134 ± 10%
a_6	1.273 ± 2%	1.168 ± 2%	1.095 ± 2%	1.126 ± 2%
		(NOTE: Covariance accuracy of coefficients assumes T_A accuracy of 0.5K)		
b_{71}	-2.9E-06	-2.6E-06	0.0E-06	-2.4E-06
b_{72}	0.000966	0.000855	0.000226	0.000812
b_{81}	2.75524	0	0	0
b_{82}	-656.37	148.96	207.71	163.10
b_{91}	0.06504	0	0	0.018974
b_{92}	-20.63	-0.62	-1.40	-6.31
		(NOTE: A zero indicates marginal instrument temperature dependence)		
		Equivalent cosmic background brightness temperature (K)		
T_c	2.757	2.765	2.765	2.829

form

$$\vec{x} = \mathcal{T}\vec{y} \tag{9}$$

where

$x_i = T_{Ai} - a_1 D_i T_C$, $i = 1 \cdots N$
$D_i = C_{Ai} - C_{Hi}/C_{Hi} - C_{Ci}$, $i = 1 \cdots N$
T_{Ai} is the physical temperature of the MFFH target, $i = 1 \cdots N$
T_C is the physical temperature of the sky horn target
$\vec{y}$ is the vector of coefficients to be estimated, a_2 through a_6
$\mathcal{T}$ is an $N \times 5$ matrix given by

$$\mathcal{T} = \begin{bmatrix} D_1T_{h1} & D_1T_{h-w1} & D_1T_{i1} & T_{f1} & T_{i1} \\ D_2T_{h2} & D_2T_{h-w2} & D_2T_{i2} & T_{f2} & T_{i2} \\ \vdots & \vdots & \vdots & \vdots & \vdots \\ D_NT_{hN} & D_NT_{h-w}N & D_NT_{iN} & T_{fN} & T_{iN} \end{bmatrix}. \tag{10}$$

The vector of coefficients, $\vec{y}$, is estimated from the data by minimum squared error inversion of (9)

$$\vec{y} = (\mathcal{T}^\dagger \mathcal{T})^{-1} \mathcal{T}^\dagger \vec{x} \tag{11}$$

where $\dagger$ denotes the matrix transpose operation.

Preliminary analysis of the T/V data revealed a strong coupling between the coefficients a_2 and a_3. These coefficients account for thermal emission by the sky horn and its connecting waveguide. This coupling may be due to either a strong temperature coupling, a relatively low insertion loss for one of the two components, or both. Its negative effect on the regression analysis was eliminated by substituting a single unknown coefficient for the two in the multi-linear regression and using the average physical temperature of the two components. (The coefficients reported below for a_2 and a_3 are each half the retrieved coefficient.) The retrieved coefficients and RSS covariance estimates of coefficient accuracy for each TMR channel are given in Table IV.

b. Linear estimate of cold sky temperature sensitivity: Calibration runs were made with the sky horn target temperature at both 80°K and ambient. This is especially important because the cold space temperature seen by the horn in flight will be significantly different (≈2.7°K), which implies a significant extrapolation of the pre-flight conditions.

Equation (6) can be rewritten, to regress against coefficient a_1, as

$$\begin{aligned} T_A - D(a_2T_h + a_3T_{h-w} + a_4T_i) - a_5T_h - a_6T_i \\ = a_1DT_c + b \end{aligned} \tag{12}$$

where

$$D = \frac{C_A - C_H}{C_H - C_C}$$

and b is a possible offset term. The coefficients a_1 estimated for each TMR channel from this regression are given in Table IV.

c. Temperature dependent nonlinear correction: Using (6) and calibration coefficients a_1–a_6, T_A can be estimated from the digital counts for each calibration run and compared with the "true" antenna temperature as determined by the temperature of the MFFH target. Fig. 8 plots this comparison for the 18 GHz TMR channel, with instrument temperature as a parameter. The error between the true and estimated antenna temperatures is plotted vs. the true antenna temperature to illustrate the nonlinear behavior of the electronics. At each instrument temperature, a quadratic curve can be seen. The magnitude of the curvature, the base of the parabola, and its vertical offset all vary with instrument temperature. One possible mechanism for this behavior is the temperature dependence of amplifier gain. Gain typically increases with decreasing temperature. Higher gain would increase the power

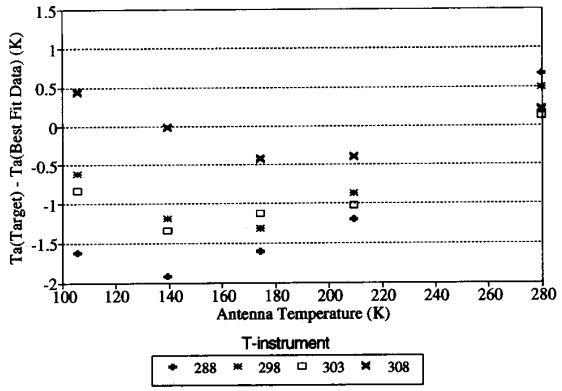

Fig. 8. 18 GHz residual error in the T_A algorithm without a correction for instrument nonlinearity.

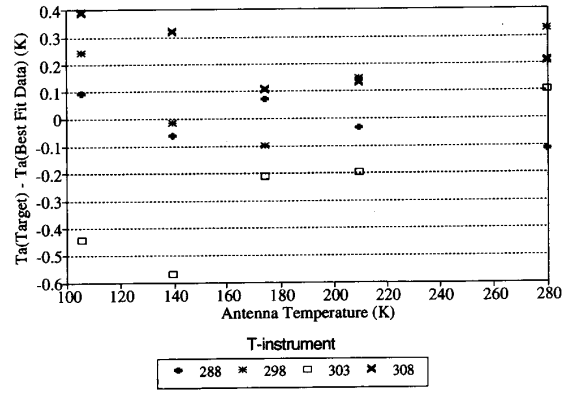

Fig. 9. 18 GHz residual error in the T_A algorithm with a temperature dependent quadratic correction included for the instrument nonlinearities.

level incident on subsequent amplifiers and on the detector diode, driving them further from their linear power region. The quadratic curvature is seen in the figure to be larger at lower temperatures, confirming this behavior. Another possible cause of the observed nonlinearity is the RF leakage between ports of the calibration ferrite switch. Leakage will add a small fraction of T_A onto the measurement of T_H, which results in a T_A dependent gain and offset. Both sources of nonlinearity are consistent with the behavior observed during T/V testing, and the correction described below should remedy either one.

Data analysis consisted of minimizing the error between the estimated and true antenna temperatures by adjusting the curvature, offset, and base of the quadratic component of error and then adding this to the estimated antenna temperature. This is the correction described by (7). Because the nonlinearity was temperature dependent, the optimal quadratic coefficients were determined independently at each instrument temperature. Linear fits of each of the quadratic correction terms to instrument temperature were performed for all TMR channels. The resulting calibration coefficients are given in Table IV.

TABLE V
ANTENNA TEMPERATURE CALIBRATION ERROR BUDGET
(All values in units of K)

	TMR Frequency (GHz) 18	21H	21V	37
Stochastic Noise	0.26	0.27	0.27	0.27
Digitization, Temp. Sensor error, and T_C error	0.18	0.18	0.18	0.18
T_A model residual	0.24	0.24	0.19	0.19
RSS T_A Precision	0.40	0.40	0.38	0.38
In-flight T_A Bias	0.40	0.40	0.38	0.38
RSS T_A Accuracy	0.57	0.57	0.54	0.54

C. Antenna Temperature Calibration Error Analysis

The residual error in the fully calibrated antenna temperature is plotted in Fig. 9 for the 18 GHz TMR channel. Performance at 21 and 37 GHz was similar The RMS residuals are 0.24°, 0.24°, and 0.19°K at 18, 21, and 37 GHz, respectively. Comparison of Fig. 9 with Fig. 8 shows that systematic instrument temperature dependent and T_A dependent effects have been largely removed by the nonlinearity correction. The RMS residual has also been lowered, by 0.98°,0.59°, and 0.55°K in an RSS sense, at 18, 21, and 37 GHz, respectively. These values can be thought of as the degree of nonlinearity present in the TMR system transfer function.

The precision of the T_A calibration in flight due to measurement noise is found from an RSS combination of the individual error terms in (6). The small contribution from the quadratic correction term can be neglected. If ΔT_A is the RMS precision in the estimate of T_A, then

$$\Delta T_A^2 = \Delta T^2 + \Delta C^2 \left[\left(\frac{\partial T_A}{\partial C_A} \right)^2 + \left(\frac{\partial T_A}{\partial C_H} \right)^2 + \left(\frac{\partial T_A}{\partial C_C} \right)^2 \right] + \Delta T_c^2 \left(\frac{\partial T_A}{\partial T_C} \right)^2 + \Delta T_n^2 \left[\left(\frac{\partial T_A}{\partial T_h} \right)^2 + \left(\frac{\partial T_A}{\partial T_{h-w}} \right)^2 + \left(\frac{\partial T_A}{\partial T_I} \right)^2 + \left(\frac{\partial T_A}{\partial T_f} \right)^2 \right] \quad (13)$$

where $\Delta T \approx 0.27$°K is the radiometer noise floor, ΔC = 1/2 count is the quantization error, ΔT_C is the uncertainty in the cosmic background brightness temperature, and ΔT_n = 0.05°K is the measurement accuracy of the platinum temperature sensors. The first term (ΔT) is found to dominate the others, and the total RSS error is $\Delta T_A \approx 0.32$°K. The net precision of the T_A calibration is an RSS combination of the ΔT_A measurement precision with the model accuracy of the T_A calibration algorithm, as determined by the T/V test residuals at the four TMR frequencies. This results in a 0.38–0.40°K residual error. The errors associated with antenna temperature calibration are summarized in Table V.

The 0.4°K RSS T_A residuals should be thought of as measures of repeatability and precision in the T_A retrieval

algorithm. Systematic offsets between the MFFH target temperature and the true antenna temperature will not be corrected. Possible sources of these systematics include: 1) differences between the arithmetic average of the temperatures of the eight thermistors distributed across the MFFH target and the MFFH beam-averaged temperature actually sensed by the TMR; 2) Local and/or global deviations of the "black body" target's emissivity from unity; and 3) MFFH far sidelobe and backlobe contributions to the true antenna temperature. These error sources are all probably small, but are also all probably on the same order as the final RMS residuals quoted here, and should, therefore, not be ignored. We conservatively estimate these additional errors to be equal in magnitude to the residual T/V errors, resulting in a RSS total T_A error of 0.54–0.57 °K for the three TMR channels.

A final correction to the TMR calibration is planned after launch which will nominally adjust each channel by a constant offset [17]. This correction will be based on coincident measurements of the downwelling brightness temperature from the atmosphere made by upward looking WVR's during T/P overpasses of island sites. This calibration will, in part, correct for the systematics present in the T_A calibration algorithm. Other possible systematic offsets, e.g. in the brightness temperature calibration algorithm [4], will also be corrected at this time. The post-launch calibration effort is estimated to result in path delay retrievals which are accurate to 1.20 cm. This corresponds to a brightness temperature accuracy of 0.71–0.77°K and a T_A accuracy of 0.54–0.57°K.

ACKNOWLEDGMENT

The authors wish to acknowledge the assistance of K. Warfield of the Jet Propulsion Laboratory with the performance and analysis of the radome material UV tests.

REFERENCES

[1] G. Carlisle, A. DiCicco, H. M. Harris, A. Salama, and M. Vincent, "TOPEX/POSEIDON project mission plan," Document D-6862 Rev. B, Jet Propulsion Lab., Pasadena, CA, 1991.

[2] C. M. Rush, "Ionospheric radio propagation models and predictions—A mini-review," *IEEE Trans. Antenna Propagat.*, vol. AP-34, pp. 1163–1170, 1986.

[3] J. Saastamoinen, "Atmospheric correction for the troposphere and stratosphere in radio ranging of satellites," in *Geophysical Monograph #15*. Washington, DC: William Byrd Press, 1972.

[4] M. A. Janssen, C. S. Ruf, and S. J. Keihm, "TOPEX/Poseidon microwave radiometer (TMR): II. Antenna pattern correction and brightness temperature algorithm," *IEEE Trans. Geosci. Remote Sensing*, vol. 33, pp. 138–146, Jan. 1995.

[5] B. D. Tapley, J. B. Lundberg, and G. H. Born, "The Seasat altimeter wet tropospheric range correction," *J. Geophys. Res.*, vol. 87, pp. 3213–3220, 1982.

[6] E. G. Njoku, J. M. Stacey, and F. T. Barath, "The SeaSat scanning multichannel microwave radiometer (SMMR): Instrument description and performance," *IEEE J. Ocean. Eng.*, vol. OE-5, pp.100–115, 1980.

[7] D. Prabhakara, H. D. Chang, and A. T. C. Chang, "Remote sensing of precipitable water over the oceans from Nimbus 7 microwave measurements," *J. Appl. Meteorol.*, vol. 21, pp. 59–68, 1982.

[8] R. Stewart, L.-L. Fu, and M. Lefebvre, "Science opportunities from the TOPEX/Poseidon mission," Rep. 86-18, Jet Propululsion Lab., Pasadena, CA, 1986.

[9] D. F. Zimbelman and A. J. Busalacchi, "The wet tropospheric range correction: Product intercomparisons and the simulated effect for tropical Pacific altimeter retrievals," *J. Geophys. Res.*, vol. 95, no. 3, pp. 2899–2922, 1990.

[10] D. Jourdan, C. Boissier, A. Braun, and J.F. Minster, "Influence of wet tropospheric correction on mesoscale dynamic topography as derived from satellite altimetry," *J. Geophys. Res.*, vol. 95, no. 10, pp. 17,993–18,004, 1990.

[11] ERS-DC Project Office, "Along track scanning radiometer and microwave sounder," Ref. DC-HO-PST-SY-008, Farnborough, Hants, U.K., 1987.

[12] E. G. Njoku, E. J. Christensen, and R. E. Cofield, "The Seasat scanning multichannel microwave radiometer (SMMR): Antenna pattern corrections—Development and implementation," *IEEE J. Ocean. Eng.*, vol. OE-5, pp. 125–137, 1980.

[13] P. N. Swanson and A. L. Riley, "The SeaSat scanning multichannel microwave radiometer (SMMR): Radiometric calibration algorithm development and performance," *IEEE J. Ocean. Eng.*, vol. OE-5, pp. 116–124, 1980.

[14] A. S. Milman and T. T. Wilheit, "Sea surface temperature from the scanning multichannel microwave radiometer on Nimbus 7," *J. Geophys. Res.*, vol. 90, no. 11, pp. 631–11, 641, 1985.

[15] E. A. Francis, "Calibration of the Nimbus 7 SMMR," M.S. thesis, Dept. Oceanography, Oregon State Univ., Corvalis, 1987, p. 248.

[16] C. S. Ruf, S. J. Keihm, B. Subramanya, and M. A. Janssen, "TOPEX/Poseidon microwave radiometer performance and in-flight calibration," accepted for publication in *J. Geophy. Res.—Oceans*, 1994.

[17] S. J. Keihm, M. A. Janssen, and C. S. Ruf, "TOPEX/Poseidon microwave radiometer (TMR): III. Wet troposphere range correction algorithm and prelaunch error budget," *IEEE Trans. Geosci. Remote Sensing*, vol. 33, pp. 147–161, Jan. 1995.

[18] F. J. Wentz, "Measurements of oceanic wind vector using satellite microwave radiometers," *IEEE Trans. Geosci. Remote Sensing*, vol. 30, pp. 960–972, 1992.

[19] J. R. Birch, J. D. Dromey, and J. Lesurf, "The optical constants of some common low-loss polymers between 4 and 40 cm^{-1}," *Infrared Phys.*, vol. 21, pp. 225–228, 1981.

[20] Emerson & Cuming, "EccoFoam® PP," Tech. Bull. 6-2-4B, Rev. 8/76, 1976.

[21] K. Green, personal communication, 1988.

Christopher S. Ruf (S'85–M'87–SM'92) received the B.A. degree in physics from Reed College, Portland, OR, in 1982 and the Ph.D. degree in electrical and computer engineering from the University of Massachusetts at Amhurst in 1987.

He worked as a Research Assistant for the Microwave Remote Sensing Society at the University of Massachusetts from 1983 to 1987, involved with microwave radar and radiometer instrumentation and inversion techniques. He continued at this institution during 1987–1988 as a Visiting Professor and Research Engineer. He then joined the technical staff at the Jet Propulsion Laboratory, Pasadena, CA in July 1988. While at JPL, he was involved with the TOPEX Microwave Radiometer as instrument scientist and algorithm development team member. He left JPL to join the faculty of the Department of Electrical and Computer Engineering at The Pennsylvania State University as an Assistant Professor in December 1991. His current research activities include a continued involvement with the TOPEX/Poseidon mission, work on the GEOSAT Follow-On Water Vapor Radiometer, instrumentation and inversion techniques for multi-sensor atmospheric remote sensing, and investigations in synthetic aperture interferometric microwave radiometry.

Dr. Ruf is an associate editor of *Radio Science* and associate editor for University Profiles in the IEEE Geoscience and Remote Sensing Society *Newsletter*. He is a member of the AGU and Commission F of the URSI. He also serves on the American Institute of Aeronautics and Astronautics Space Based Observations System Subcommittee on Passive Microwave Sensor Calibration.

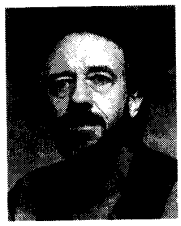

Stephen J. Keihm received the B.S. degree in physics from Fordham University, Bronx, NY, in 1968, the B.S. degree in mechanical engineering from Columbia University, New York, in 1969, and the M.S. degree in astronautical science from Stanford University, CA, in 1970.

From 1970 to 1978, he worked as a Research Assistant, then Staff Associate at the Lamont-Doherty Geological Observatory of Columbia University. While at Lamont, he served as co-investigator for the Apollo 15 and 17 lunar heat flow experiments, and principal investigator in studies of the thermal and electrical properties of the lunar regolith. In 1978, he joined the Planetary Science Institute, Pasadena, CA, doing theoretical studies for the interpretation of data from the remote sensing of planetary surfaces. Since 1982, he has worked as a Contractor Employee for the Jet Propulsion Laboratory, Pasadena, CA. At JPL, he has developed lunar microwave calibration models for the Cosmic Background Explorer (COBE) experiment, and worked extensively in the areas of algorithm development and data interpretation for Earth-based aircraft, and satellite microwave measurements of the atmosphere and sea surface. His current research activities include design and algorithm development for future satellite microwave instruments and the development of an advanced ground-based water vapor radiometer for tropospheric path delay calibration in the Cassini gravity wave experiment.

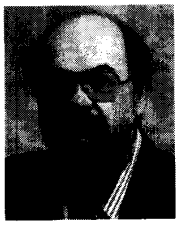

Michael A. Janssen received the B.A. in physics in 1963 and the Ph.D. degree in atmospheric and space sciences in 1972 from the University of California, Berkeley.

He has been with the Jet Propulsion Laboratory in Pasadena, CA since 1972, first as a NASA National Research Council Resident Research Associate, and since 1974 as a Member of the technical staff. He has been involved in many aspects of radio astronomy and microwave remote sensing, including the microwave remote sensing of the atmospheres of Earth and other planets, the development of ground-and space-based radiometers for astrophysics and remote sensing, and observational cosmology. He is a member of the Cosmic Background Explorer (COBE) science working group and the Cassini radar science team. He recently served a term as Manager of the Space Physics and Astrophysics Section of JPL's Earth and Space Sciences Division, and currently heads the Astrophysics effort in that division.

Dr. Janssen is a member of Phi Beta Kappa, the American Astronomical Society, the International Union of Radio Science, the International Astronomical Union, and the American Geophysical Union. He was awarded the NASA Exceptional Scientific Achievement Medal in 1992 for his contributions to COBE.